processes

MDPI

Article

Transient Characteristics of Three-Dimensional Flow in a Centrifugal Impeller Perturbed by Simple Pre-Swirl Inflow

Ze Wang and Wei Zhang *

Key Laboratory of Fluid Transmission Technology of Zhejiang Province, Zhejiang Sci-Tech University, Hangzhou 310018, China
* Correspondence: zhangwei@zstu.edu.cn

Abstract: The pre-swirl inflow generated by guide vanes could improve the hydrodynamic performances of centrifugal pumps as long as the inflow matches the patterns of internal flow of the impeller. In this work, we present a numerical investigation on the internal flow in a centrifugal impeller subjected to inflow artificially constructed with simple pre-swirling; unsteady Reynolds-Averaged Navier-Stokes (URANS) simulations are performed at the designed flow rate with five values of rotating velocity of the inflow, i.e., U_{rot}/U_{ref} = −0.5, −0.3, 0.0, 0.3 and 0.5, where U_{rot} and U_{ref} denote the rotating and normal velocity component at the entrance of the inflow tube, respectively. The primary objective of this work is to reveal the three-dimensional characteristics of internal flow of the impeller as influenced by the superimposed pre-swirl inflow, and to identify the propagation of inflow within the impeller. The numerical data are presented and analyzed in terms of the streamline fields, the distributions of various velocity components along the circumferential and axial directions, the pressure distribution and limiting streamlines on the surfaces of a blade. Numerical results reveal that separation occurs around the leading edge of the blades and occasionally at the trailing edge, and the internal flow is more uniform in the central region of the channels. A noticeable fluctuation of both radial and circumferential velocities is observed at the outlet of the impeller as it is subjected to counter-rotating inflow, and the greatest fluctuation is close to the hub instead of the middle channel and shroud as for the co-rotating inflow. The boundary layer flow of suction surface is more sensitive to the inflow; occasional small-scale separation bubble occurs on the suction surface around the leading edge for some blades, and reattachment of separated flow is reduced for the counter-rotating inflow.

Keywords: centrifugal impeller; pre-swirl inflow; three-dimensional flow; separation

Citation: Wang, Z.; Zhang, W. Transient Characteristics of Three-Dimensional Flow in **a** Centrifugal Impeller Perturbed by Simple Pre-Swirl Inflow. *Processes* **2022**, *10*, 2007. https://doi.org/10.3390/pr10102007

Academic Editors: Lijian Shi, Kan Kan, Fan Yang, Fangping Tang and Wenjie Wang

Received: 6 September 2022
Accepted: 27 September 2022
Published: 5 October 2022

1. Introduction

Centrifugal pumps are widely used for liquid transportation applications in many fields, such as thermal power plants, metallurgical production, and processing industries. The performances of the centrifugal pumps, i.e., head and efficiency which represent the work and loss during energy transfer, are greatly determined by the centrifugal impeller in terms of the patterns of its internal flow. Since energy transfer between the impeller and fluid is crucial for the implementation of the pumps, the characteristics of internal flow within the impeller and even the whole pump system have been investigated in many works, even for the simplest working conditions as steady and uniform fluid enters the pump. However, in a lot working circumstances, the flow patterns are rather complex as they are affected by certain influential factors, such as unsteady and/or non-uniform inflow, during a start/stop stage where the rotation speed varies, and in a multi-stage pump. The flow in the channels of the impeller may separate from the solid walls and result in separation bubbles which block the channel, and the interactions between the flows in the impeller and inflow tube or diffusers are consequently affected.

To understand the mechanisms of flow in a centrifugal impeller, a large number of numerical and experimental investigations have been carried out with the consideration of various influential factors. Byskov et al. [1,2] performed large-eddy simulation (LES) on the internal flow of a six-blade impeller for a centrifugal pump. The LES approach is capable of accurately predicting the hydrodynamic performances of the impeller and capturing the transient flow field compared with the experimental result. No significant separation is observed at designed flow rate, while notable differences are shown for flows in neighboring channels at a quarter flow rate. A steady non-rotating stall was observed at the entrance of one channel and relative vortices were observed for the rest channels. Zhang et al. [3,4] analyzed the transient evolutions of stalled structures in a low specific speed centrifugal pump based on coherent analysis of pressure signals, and presented and explored the unsteady evolution of flow and pressure pulsation in the stagnant state by using the DDES method. Krause et al. [5] and Ullum et al. [6] successfully captured the rotating stall flow using the time-resolved particle image velocimetry (PIV) technique. Zhou et al. [7,8] studied stalled flow in a centrifugal pump using LES approach. As the flow rate decreases, the stalled cell grows in size and occupies the channel. The pressure fluctuation caused by the evolution of stalled cell is analyzed, and the peak value of the pressure fluctuation at quarter designed flow rate is obviously greater than that at half designed flow rate. Pei et al. [9] carried out numerical simulations on flow in a centrifugal pump with a volute under partial load to analyze the three-dimensional periodic flow in all channels of the impeller. Li et al. [10] measured the internal flow in the impeller of a low specific speed centrifugal pump using the PIV technique to quantify the energy conversion characteristics as determined by the internal flow patterns. Westra et al. [11] analyzed the effect of secondary flow in the impeller of a low specific speed centrifugal pump with vane-less diffuser under designed and off-designed conditions.

The patterns of inflow at the entrance of the centrifugal impeller have a substantial impact on the hydrodynamic performance of the impeller, as revealed in some works. Song et al. [12] studied the influence of different pre-swirl inflows on the aerodynamic performances of the impeller in a centrifugal compressor. Xiao et al. [13] conducted numerical simulations on the internal flow of a single-stage centrifugal compressor with inflow following pre-swirl patterns; numerical results showed that the inflow pre-swirling directly affects the circumferential distribution of flow parameters in the impeller. Gish et al. [14] studied the effect of the geometry of inlet stators on the performances of a hydroturbine under different Reynolds numbers, and found the proper geometry has the potential to improve the performance. Danlos et al. [15] investigated flow in a compressor impeller and analyzed the influence of pre-swirling on the instability of the compressor system with emphasis on the surge line. Amin and Xiao [16] conducted numerical simulations on flow through a horizontal-axis tidal turbine with or without the pre-swirl stator. It was found that the velocity field around the turbine can be improved by using the pre-swirl stator, and the turbine efficiency can be increased by about 13% at a certain blade tip velocity ratio. Mohseni et al. [17] conducted numerical and experimental studies on the effect of guide blade profiles in terms of the setting angle and positive or negative inlet swirling, and found that series profiles showed better aerodynamic performance than S-profile under negative inlet swirls. Zhang et al. [18] studied the clocking effect in a multi-stage centrifugal pump in terms of the velocity field and hydrodynamic performances of the pump; it was found that at the appropriate clocking position, the guide vanes could effectively reduce the size and intensity of vortices between neighboring stages of the pump. Zhao et al. [19] applied the inlet guide vane in a centrifugal compressor to improve its performance and studied the flow patterns in the impeller. Xu et al. [20] studied the influence of chord length and installation angle of guide vanes on the efficiency and internal flow field of an axial-flow pump, and found that the efficiency can be improved under low flow rates by rotating the guide vanes in the counter-clockwise direction. Poujol et al. [21] studied the effect of staggered inlet guide vanes on the stability of a centrifugal compressor. The increased staggered angle moves the surge line towards the left, and

rotating instability occurs at a lower mass flow rate. Zhong et al. [22] experimentally tested the performance characteristics of an axial-flow pump with and without guide vanes to explore the patterns of flow in the impeller. Liu et al. [23] conducted numerical calculations using the steady and unsteady Reynolds-averaged Navier-Stokes (RANS and URANS) simulation approaches to investigate the internal flow in a centrifugal fan under the condition of incoming flow from an upstream bended inflow tube of various radii and demonstrated the effects of the non-axisymmetric pre-swirl flow generated due to the curvature of the bended inflow tube. Heidarian et al. [24] modelled shark's skin for the first time, and analyzed the effects of riblet on a submerged flat plate. Jiang et al. [25] presented a review on two phase performances from various centrifugal pumps designs, mainly based on experimental results and detected the significant geometrical parameters. Heidarian et al. [26] presented calculations on the Clark-Y wing section of the Reynolds-averaged Navier-Stokes (RANS) equations solver and verified the numerical results of lift and drag of the rectangular airfoil at ground effect. Xu et al. [27] developed a wind turbine rotor blade design and optimization method and introduced a propeller-turbine rotor code coupling aerodynamic and structural properties.

It is revealed in the above reviewed literature that the characteristics of inflow of the centrifugal impeller greatly determine the patterns of flow within the impeller and consequently the performances of the pump system. In most of the existing studies, the centrifugal impeller of the pump or compressor system is equipped with an upstream guide vane or stator system to be compatible to different working conditions, thus the pre-swirl flow is generated and the inflow of the centrifugal impeller rotates in the circumferential direction and is spatially non-uniform. It is already known that the pre-swirl inflow affects the internal flow of the impeller and determines the hydrodynamic performances of the impeller, however, the transient characteristics of the internal flow is not revealed in terms of the three-dimensionality, which represents the temporal unsteadiness and spatial non-uniformity that are crucially related with significant flow phenomena such as boundary layer separation and stall. In this work, we performed a numerical investigation on the transient flow in a centrifugal impeller at the designed flow rate under the influence of pre-swirl inflow. Different from the models in existing works where the pre-swirl flow is generated by the inlet guide vanes or a stator of specific geometry, we artificially constructed the pre-swirl flow in a simple way without the consideration of certain geometries that the inflow rotates in the circumferential direction. The benefit of this model is that the essential influence of the pre-swirl flow on the internal flow of impeller is considered, while the particular effect associated with the specific geometry or installation of guide vanes or stator is omitted, thus the present model reflects the general influence from the pre-swirl flow. The objective of our work is to demonstrate the effect of pre-swirl inflow, in both magnitude and direction, on the transient three-dimensional flow within the impeller. The three-dimensionality of the internal flow are presented and analyzed mainly in terms of the distributions of radial, circumferential and axial velocities within the channels of the impeller. Moreover, we discuss the boundary layer flow on the blade surfaces in terms of the limiting streamlines and pressure field.

The paper is organized as follows. Section 2 introduces the physical models, the formulation of the pre-swirl inflow, the numerical simulation and grid independence verification. Section 3 presents and analyzes the numerical results. Section 4 gives some conclusions.

2. Numerical Setup

2.1. Physical Model

In this work, we investigate the flow in a six-blade centrifugal impeller which is introduced in the work of Byskov et al. [1,2], as shown in **Error! Reference source not found.**a. The geometrical and operational parameters of the impeller are listed Table 1 and Table 2 respectively. Byskov et al. [2] have carried out a detailed experimental study

on the internal flow of this centrifugal impeller at designed and off-designed flow rates using the PIV technique, and the transient flow patterns are revealed and compared with the numerical data obtained by LES approach. Since our objective is to explore the patterns of flow in the impeller subjected to pre-swirl inflow, an extended inflow tube is applied upstream of the impeller to permit the development of swirling flow; its radius is the same as that of the impeller and extends in the streamwise (axial) direction for a length of 2.1 D_1. An outflow section is placed at the outlet of the impeller to prevent the occurrence of backflow; the inner and outer diameters are D_2 and 1.36 D_2, respectively, and the width is the same as that of the impeller, i.e., b_2. The computational domain is shown in Error! Reference source not found.b.

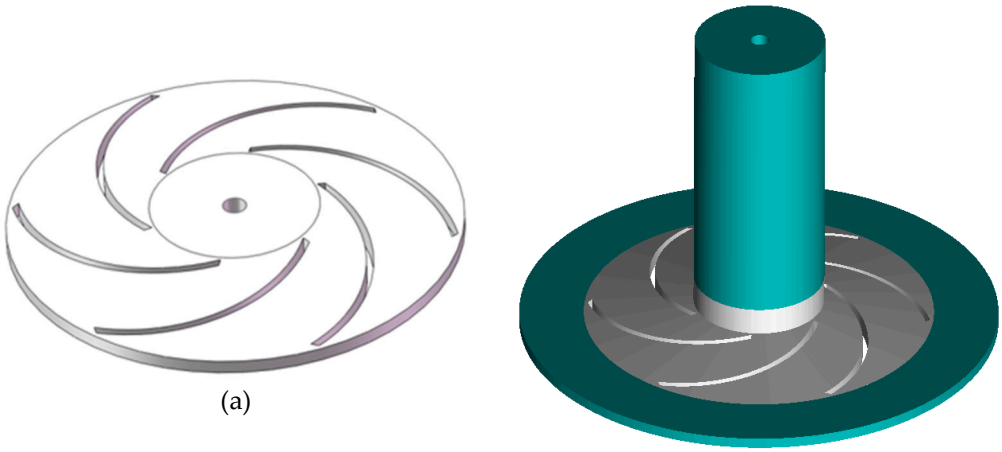

(a) (b)

Figure 1. The geometry of the centrifugal impeller; (**a**) configuration of six-blade impeller; (**b**) computational domain.

Table 1. Geometric specifications of the centrifugal impeller.

Parameter	Value
Inlet Diameter, D_1 (mm)	71.0
Outlet Diameter, D_2 (mm)	190.0
Inlet height, b_1 (mm)	13.8
Outlet height, b_2 (mm)	5.8
Blade thickness, t (mm)	3.0
Number of blades, Z	6
Inlet angle, β_1 (deg)	19.7
Outlet angle, β_2 (deg)	18.4
Blade curvature radius, Rb (mm)	70.0
Specific speed, N_s	26.3

Table 2. Flow specifications of working condition.

Parameter	Value
Q/Q_d	1.0
Flow rate, Q	3.06
Head, H	1.75
Rotation speed, n	725
Reynolds number, Re	1.4 × 106

The centrifugal impeller is geometrically axisymmetric and the blades are backward-curved, thus the direction of swirling of the inflow determines the patterns of internal

flow of the impeller. The fluid at the entrance of the inflow tube has two velocity components. The uniform streamwise velocity is along the axial direction towards the impeller whose magnitude is defined as U_{ref} as determined by the volume flow rate. The circumferential velocity defined as U_{rot} is applied perpendicular to the streamwise velocity. The direction of inflow could be either clockwise or counterclockwise, i.e., in contrary or aligned with the direction of rotation of the impeller, and is termed as counter-rotating and co-rotating inflow as exemplified in Figure 1. The magnitude of circumferential velocity is set as zero, 0.3 U_{ref} and 0.5 U_{ref}, and is represented as positive or negative depending on the direction.

Figure 1. Definition of the direction of pre-swirl inflow. The clockwise and counterclockwise directions are termed as counter−rotating and co−rotating inflows, respectively.

2.2. Numerical Methods

The time-dependent incompressible flow is governed by the conservation of mass and momentum equations [28]:

$$\frac{\partial u_i}{\partial x_i} = 0 \tag{1}$$

$$\frac{\partial u_i}{\partial t} + u_j \frac{\partial u_i}{\partial x_j} = f_i - \frac{1}{\rho}\frac{\partial P^*}{\partial x_i} + \nu \frac{\partial^2 u_i}{\partial x_j \partial x_j} \tag{2}$$

where x_i is the components of the Cartesian coordinate system; u_i is the velocity component; P^* represents the pressure considering the conversion of turbulent kinetic energy and centrifugal force; f_i is the component of volume force.

Since the SST k-ω turbulence model [29] has good results in the simulation of boundary layer flows near the wall [30], the SST k-ω turbulence model is chosen to simulate the impeller numerically in this paper. The transport equations of the turbulent kinetic energy k and the turbulent dissipation rate ω [31] are as follows:

$$\frac{\partial k}{\partial t} + \nabla \cdot (uk) = P_k - \beta^* k\omega + \nabla \cdot \left[\left(\nu + \sigma_k \nu_T \right) \nabla k \right] \tag{3}$$

$$\frac{\partial \omega}{\partial t} + \nabla \cdot (\mathrm{u}\omega) = \delta S^2 - \beta \omega^2 + \nabla \cdot \left[\left(\nu + \sigma_w \nu_T \right) \nabla \omega \right] + 2\left(1 - F\right) \frac{\sigma_{\omega 2}}{\omega} \nabla k \cdot \left(\nabla \omega \right)^T \tag{4}$$

$$\nu_T = \frac{a_1 k}{\max\left(a_1 \omega; SF_2 \right)} \tag{5}$$

where $P_k = \min\left[\nu_T(\nabla \times u)\cdot(\nabla \times u)^T, 10\beta^* k\omega\right]$, S is the absolute value of the vorticity. The constants of the SST k-ω turbulence model in the present study [32] are: $\sigma_{k1} = 0.85$, $\sigma_{k2} = 1.0$, $\sigma_{\omega 1} = 0.5$, $\sigma_{\omega 2} = 0.856$, $\beta_1 = 0.075$, $\beta_2 = 0.0828$, $\alpha_1 = 0.31$, $\delta_1 = 0.5532$, $\delta_2 = 0.440$, $\beta^* = 0.09$.

In this work, the simulations are performed for the centrifugal impeller operated under designed flow rate $Q_d = 3.06$ L/s, which is used to compute the magnitude of streamwise velocity imposed at the entrance of the inflow tube (U_{ref}). The UDF program is set in the inlet boundary condition to control the rotation direction of the fluid. The circumferential velocity of the inflow is set as $U_{rot}/U_{ref} = -0.5, -0.3, 0.0, 0.3$ and 0.5 in which the value of 0.0 denotes zero-swirling inflow. Zero gauge pressure is set at the outlet of the outflow section. No-slip condition is applied for velocity components on all solid walls.

The unsteady Reynolds-averaged Navier-Stokes (URANS) simulations were performed using ANSYS-Fluent. The governing equations are discretized by second-order central difference scheme in space and second-order implicit scheme in time. The SIMPLEC algorithm is used to decouple the solutions of velocity and pressure. The time step size of the unsteady simulation is fixed at 2.3×10^{-4} s as the impeller rotates for one degree. The maximum number of iterations in one physical step is 20 and the convergence criterion of all equation is 10^{-5}. To ensure the fully development of flow within the impeller, we first carried out the simulation for ten revolutions of the impeller, and subsequently the production simulation as the impeller rotates for another revolution that the results are saved for following analysis and discussions.

2.3. Grid Sensitivity Study

The structured grid of the model is generated using ANSYS-ICEM CFD, as shown in Figure 2a. To resolve the boundary layer flow, the grid is refined in the near-wall region of all solid walls especially around the leading and trailing edges of the blades, as given in Figure 2b,c. The value of y+ on the surfaces of blade, shroud and hub is generally lower than 10, and is slightly higher as <15 at the outlet of impeller.

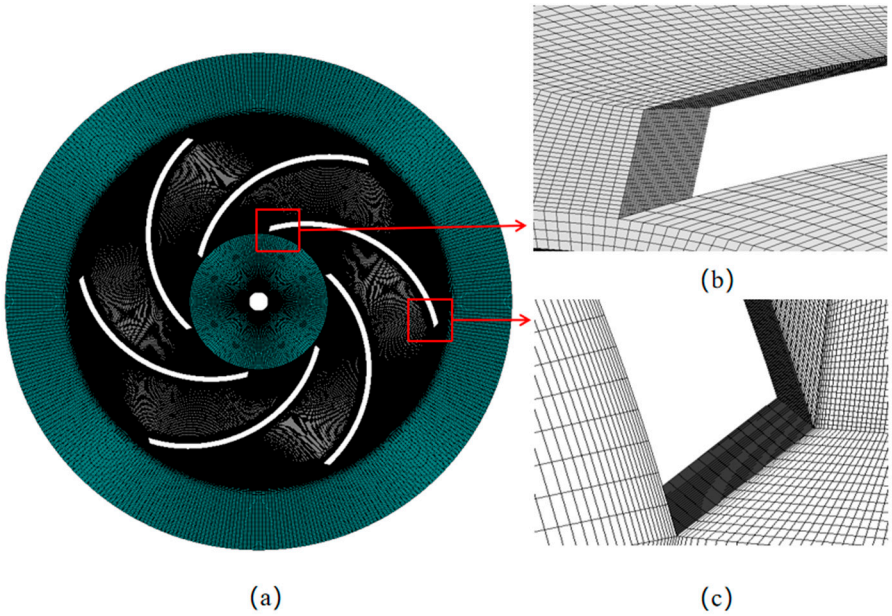

Figure 2. (a) Gird of the whole model; (b) enlarged view at the leading edge of the blade; (c) enlarged view at the trailing edge of the blade.

We performed grid sensitivity study to evaluate the influence of grid number on the accuracy of simulation results. Four sets of grids are generated and the head of the impeller for the zero-swirling inflow case is calculated and listed in **Error! Reference source not found.**. It is seen that the relative difference is less than 5% for grid 3 and the experimental

data. To balance the computational cost and numerical accuracy, we chose to use grid 3 for following simulations.

Table 3. Head of the impeller obtained using different number of grid.

	Grid Number	Head
Grid 1	4,740,324	2.42
Grid 2	5,598,924	2.51
Grid 3	7,642,362	2.31
Grid 4	9,185,268	2.38
Experiment [2]		2.41

3. Results and Discussion

3.1. Development of Pre-Swirl Inflow

Although swirling is imposed at the entrance of the inflow tube, the circumferential velocity of the inflow, representing the intensity of swirling, is attenuated during its motion into the interior of the finite-length tube along with the formation of boundary layer. It is necessary to quantify the intensity of pre-swirl flow at the exit of the inflow tube (inlet of the impeller). Figure 3 shows the distribution of axial and circumferential velocities in the radial direction at the exit of the inflow tube. Since the inflow tube is axisymmetric in geometry, the distributions are the same at any circumferential position. It is seen in the figure that the uniform inflow, in both axial and circumferential directions, gradually develops and presents a parabolic distribution after the fluid moves through the inflow tube. The distribution of axial velocity is obviously affected by the value of U_{rot} in that the velocity of near-wall flow close to the inner wall (shaft of the impeller) is comparably smaller at certain radial positions for the U_{rot}/U_{ref} = −0.5 and 0.5 cases. The nearly identical distributions reflect that the rotating flow in the impeller has no influence on the flow in the upstream region. The swirling of the inflow is notably attenuated as the flow develops towards the impeller. The maximum magnitude of circumferential velocity reduces to around 0.24 U_{ref} and 0.40 U_{ref} for the U_{rot}/U_{ref} = ±0.3 and ±0.5 cases, in which the difference denotes the attenuation. As the value of U_{rot} increases, the maximum magnitude of axial and circumferential velocities appears close to the outer wall of the inflow tube because of centrifugal force. The effective Reynolds number for flow near the inner wall of the tube gets lower, thus a thick boundary layer develops.

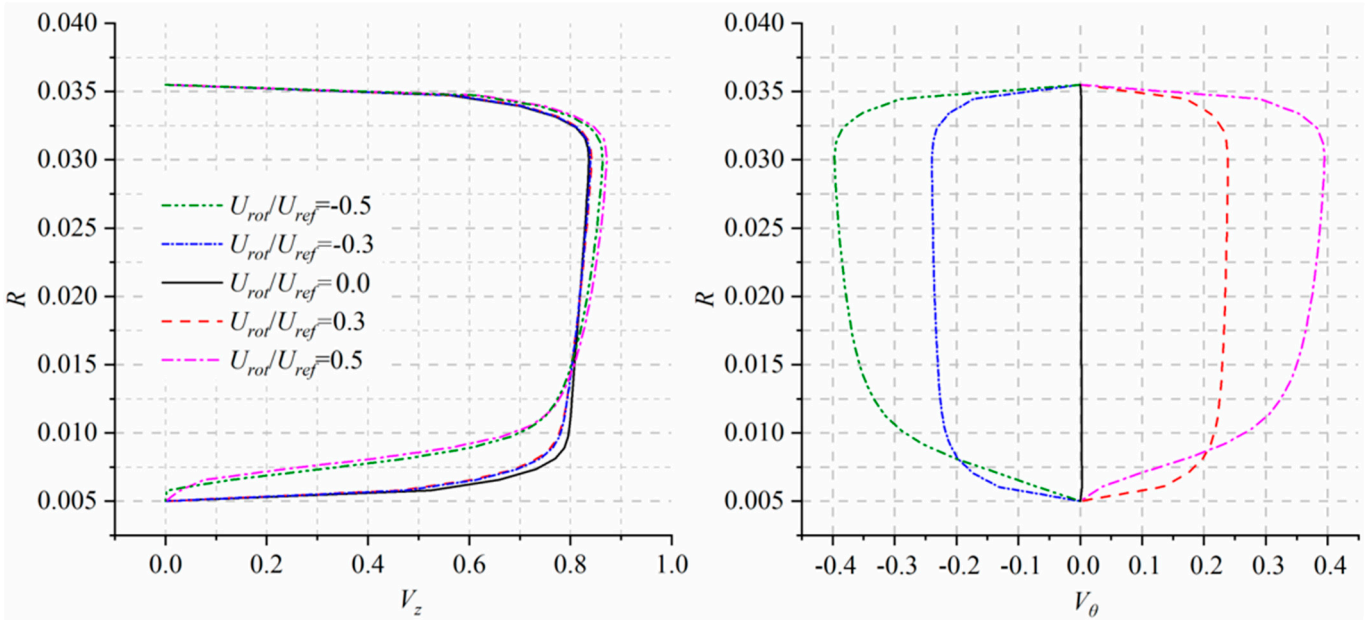

Figure 3. Distributions of axial velocity (V_z) and circumferential velocity (V_θ) at the exit of the inflow tube.

3.2. General Flow Patterns

To demonstrate the general patterns of flow in the impeller, we present the instantaneous distribution of streamlines at three axial cross-sections in Figure 4. The cross-sections are labeled as Z/b_2 = 0.1, 0.5 and 0.9 as measured from the hub of the impeller, i.e., close to the hub, at the middle and close to the shroud of the impeller. In general, the streamline field is quite similar for the several cases with different pre-swirl inflows. Small-scale vortices appear at the leading edge of the suction side of the blade, and no reversed flow is observed within the channels. On the cross-sections at Z/b_2 = 0.5 and 0.9, tiny vortices may also appear around the trailing edge of some blades. The boundary layer flow is found to detach from the pressure surface in the upstream part of the blade. As the fluid moves towards the outlet of impeller, the significant Coriolis force drives the fluid towards the pressure surface where the magnitude of velocity increases, and the flow at the outlet of impeller is getting uniform. It is observed that for co-rotating inflow (U_{rot} < 0), the detachment of boundary layer flow on the pressure surface is relatively weak compared with the counter-rotating inflow (U_{rot} > 0) cases, especially for the Z/b_2 = 0.1 cross-section.

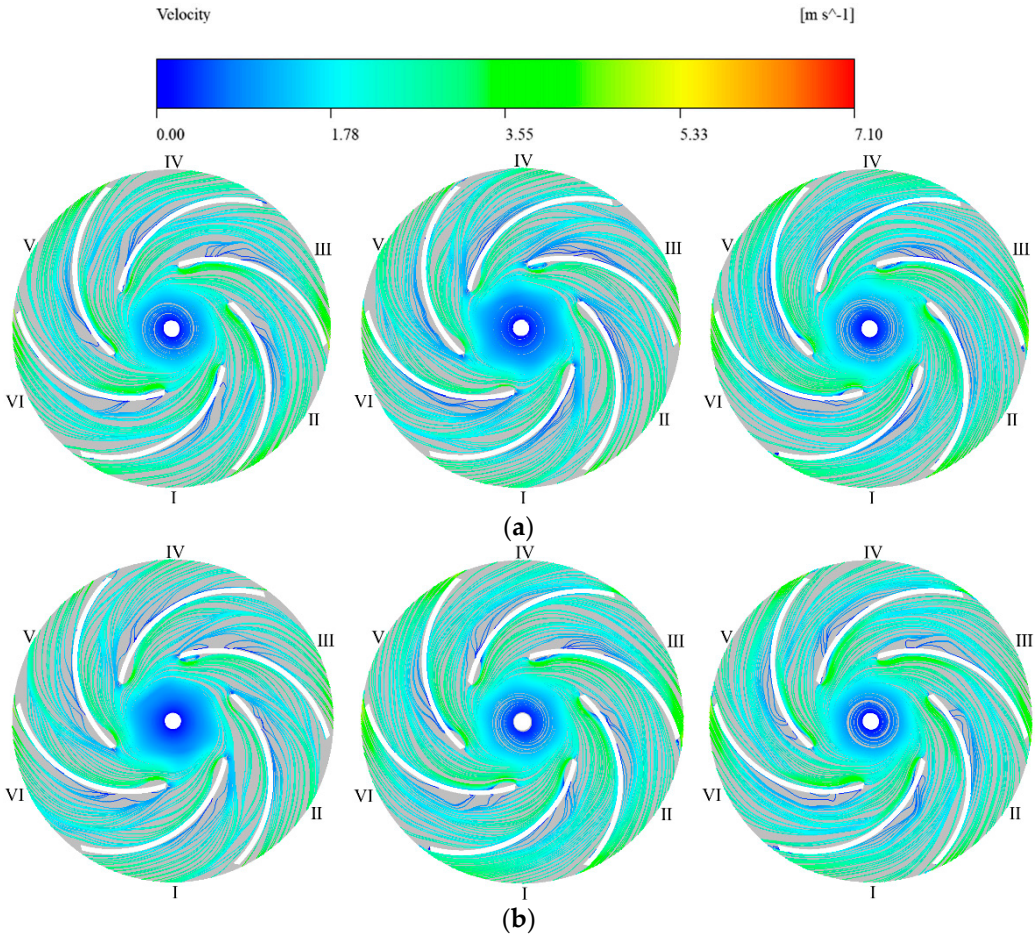

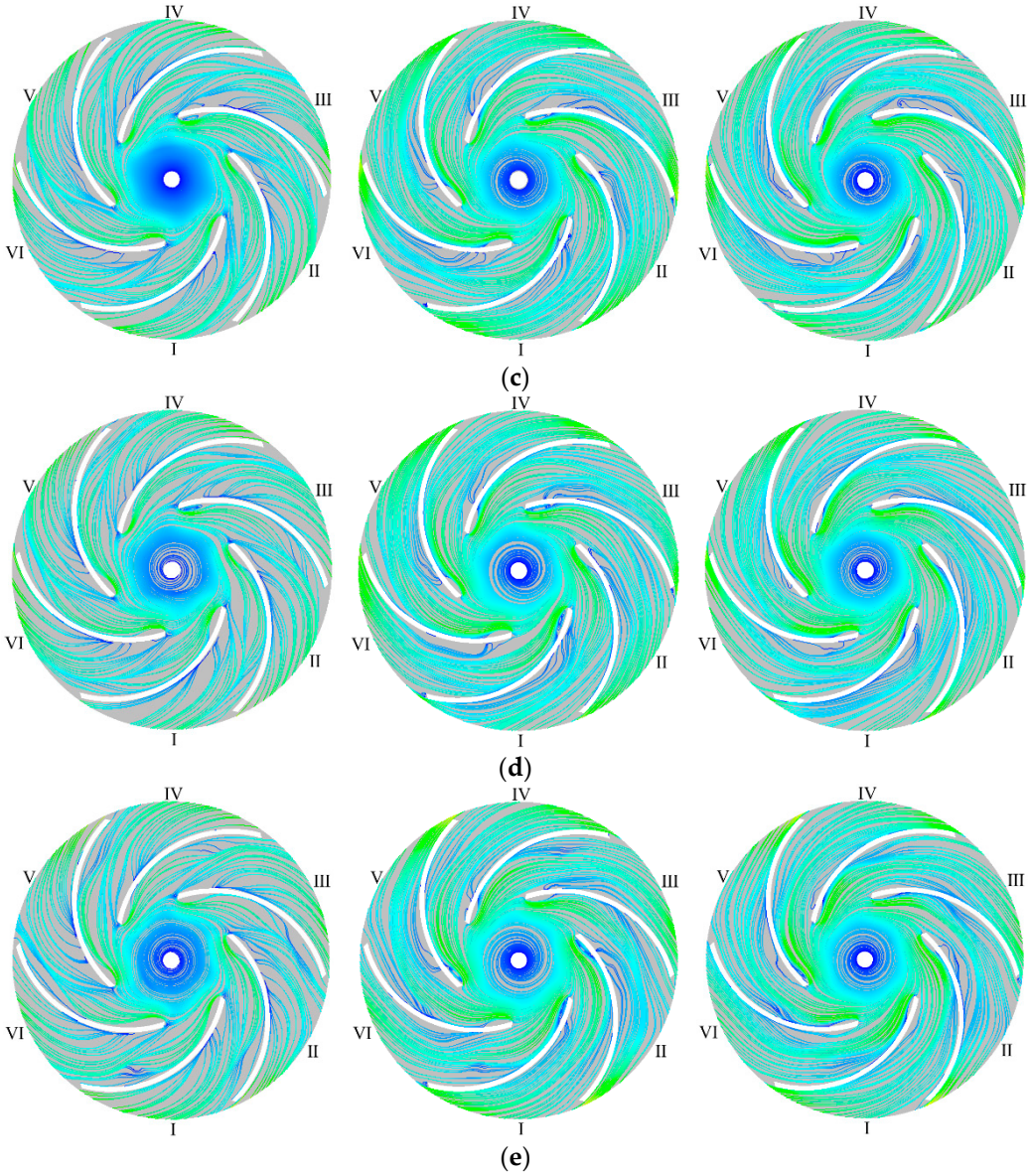

Figure 4. Distribution of instantaneous streamlines for (from top to bottom): U_{rot}/U_{ref} = −0.5 −0.3, 0.0, 0.3 and 0.5. The left, middle and right columns represent the distributions on the cross-sections at Z/b_2 = 0.1. 0.5 and 0.9, respectively.

3.3. Three-Dimensional Flow: Blade-to-Blade Distribution

The three-dimensionality of internal flow of the impeller is presented and analyzed by the blade-to-blade distribution of velocity components. We define the normalized radial position as $r^* = (r - r_1)/(r_2 - r_1)$ in which r_1 and r_2 are the radii of inlet and outlet of the channels, respectively. Three radial positions for the cross-sections are chosen for further analysis which locate at the inlet, middle and outlet of the channels, i.e., r^* = 0.0, 0.5 and 1.0, as exemplified in Figure 5. The distributions of normalized radial velocity V_r in the circumferential direction across all channels are presented in Figure 6. The curves are obtained at the intersection line formed by the axial cross-section at Z/b_2 = 0.5 and the respective constant-r^* cross-section, and for six moments during the impeller rotates for 60° which is termed as period T. The distributions are generally similar at the leading edge of blades for cases of inflows of different swirling, and the temporal fluctuation is minor as observed by the overlapping curves. The magnitude of V_r reduces substantially at the middle and outlet of the channels because of the diverging of the channel, and significant temporal fluctuation is seen for all channels.

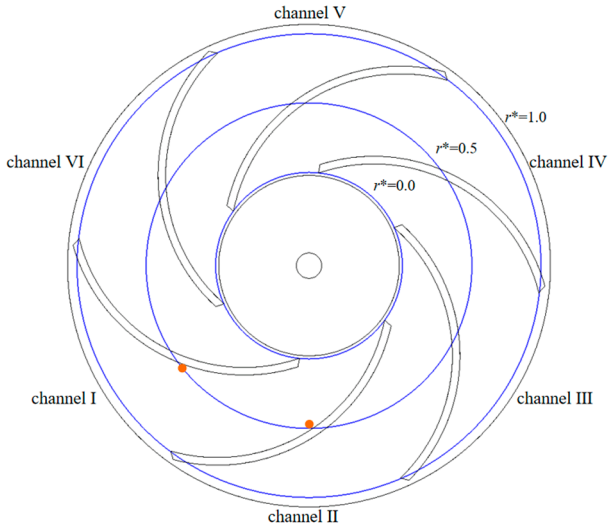

Figure 5. Definitions of radial cross-sections at r* = 0.0, 0.5 and 1.0.

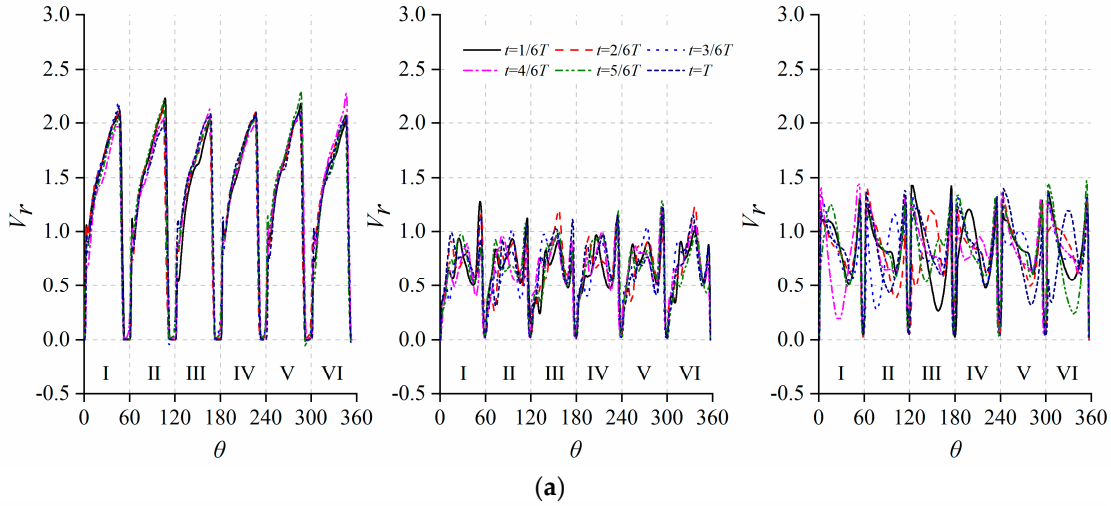

(**a**)

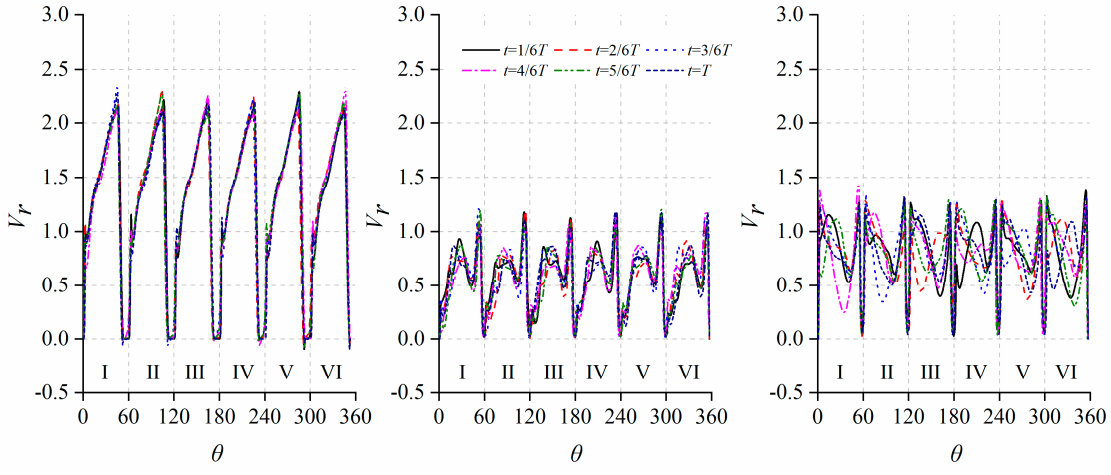

(**b**)

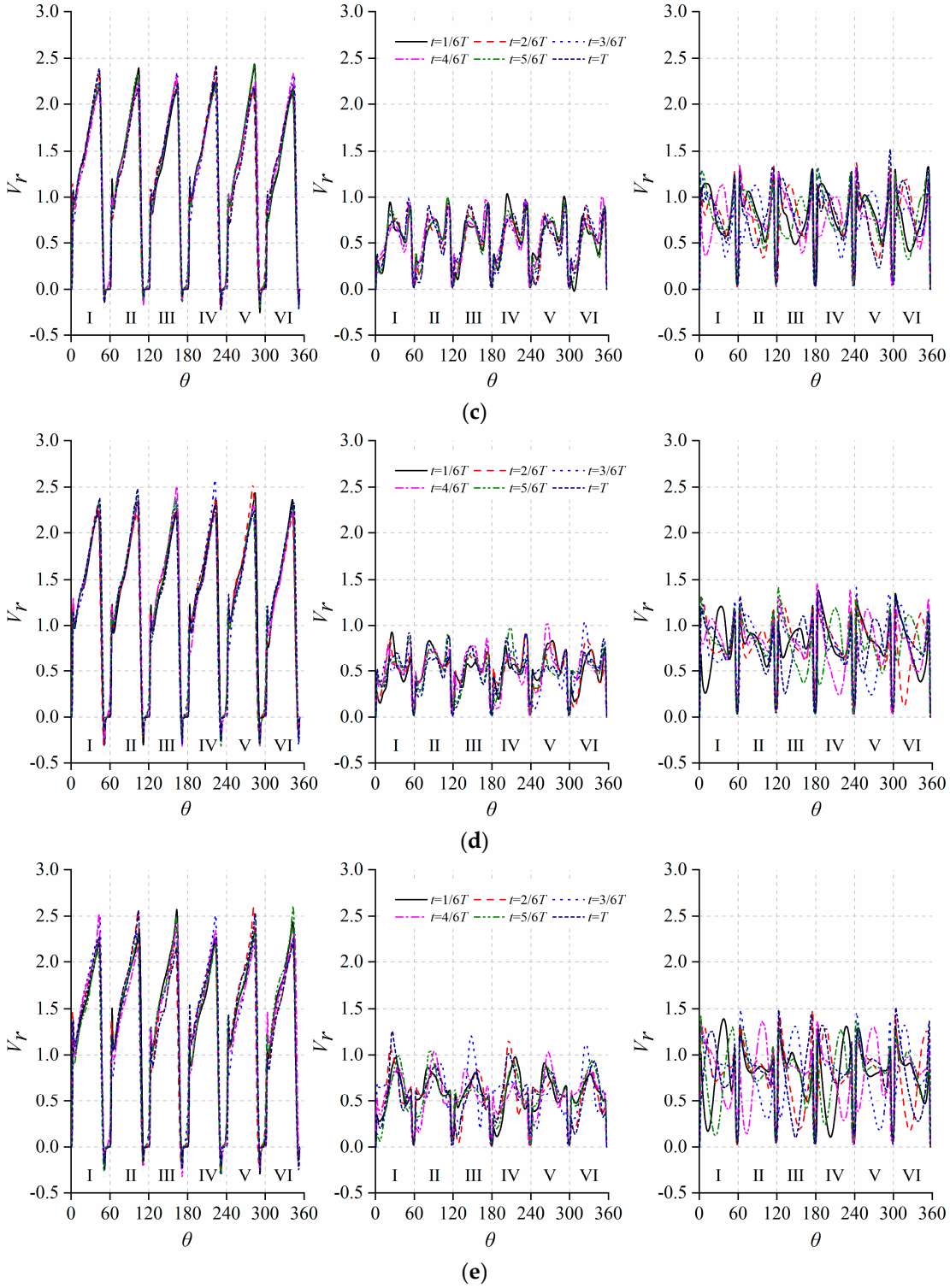

Figure 6. Distributions of instantaneous normalized radial velocity along the circumferential direction at r* = 0.0 (left), r* = 0.5 (middle) and r* = 1.0 (right) for (from top to bottom) U_{rot}/U_{ref} = −0.5, −0.3, 0.0, 0.3 and 0.5.

The distribution of V_r around the leading edge of the blades (r* = 0.0) is quite similar for the several channels. The magnitude of V_r gradually increases from the pressure surface and abruptly decreases close to the suction surface, and could even be negative as a result of the formation of vortices for cases of zero-swirling (U_{rot} = 0.0) and counter-rotating (U_{rot} > 0) inflows, and the reversed flow is more obvious for the U_{rot} = 0.3 and 0.5 cases.

For co-rotating inflow cases, the peak magnitude of Vr observed near the suction surface gets smaller compared with other cases.

In the middle of the channels (r* = 0.5), the flow within the same channel is more non-uniform and the temporal fluctuation is strong. There is both abrupt increasing and decreasing close to the pressure and suctions surfaces of the blades, while an additional fluctuation appears at the center of the channel for all cases. It is observed that as U_{rot} increases from negative to positive, i.e., from co-rotating to counter-rotating inflow, the position for the peak magnitude of V_r moves from the suction surface to pressure surface for all channels, and the fluctuating amplitude at any circumferential position greatly increases, reflecting stronger unsteady behaviors of internal flow.

The temporal fluctuation of V_r at the outlet of the impeller (r* = 1.0) is much stronger than flow in the center of the channels. Except for the drastic variation in velocity magnitude on the surfaces of the blades, the internal flow in the central region of all channels exhibits significant temporal variation. It is seen that the magnitude of V_r varies a lot especially for inflow with strongly swirling inflow U_{rot}/U_{ref} = ±0.5, while the position of the peak magnitude also moves in time, although the motion is asynchronous for the various channels. The magnitude of V_r is greatly different for flow in various channels. In the case of U_{rot}/U_{ref} = 0.3, abnormal fluctuation of V_r is found in channel-I and channel-II with mild fluctuation and relatively small peak magnitude, especially in channel-II.

The three-dimensionality of flow from a blade-to-blade view is further presented and analyzed by the distribution of circumferential velocity V_θ on the intersecting lines between the axial cross-section at Z/b_2 = 0.5 and radial cross-sections at r* = 0.0, 0.5 and 1.0, as shown in Figure 7. The flow is quite stable and there is almost no temporal variation in velocity magnitude at the inlet of channels, and the distribution is quite similar for the various channels. A minor fluctuation is observed at the middle of the channels, and the largest magnitude reduces; the distribution is still similar for the various channels. Great fluctuations form at the outlet of the channels especially in the central region.

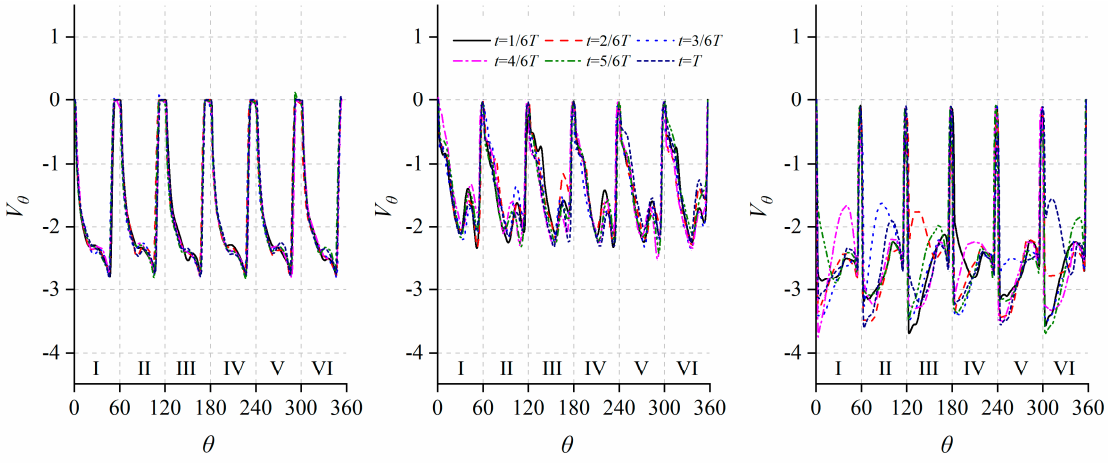

(**a**)

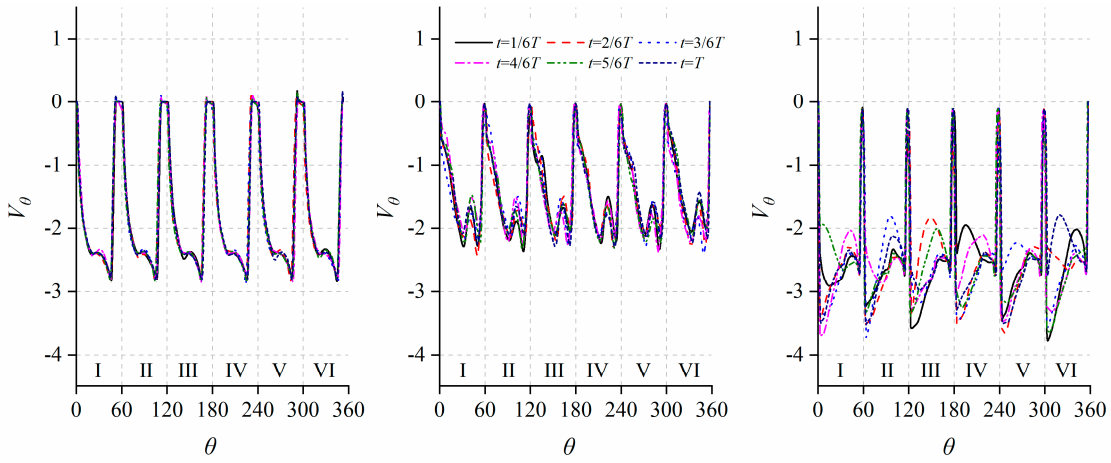
t=1/6T t=2/6T t=3/6T
t=4/6T t=5/6T t=T
V_θ
I II III IV V VI
0 60 120 180 240 300 360
θ

(**b**)

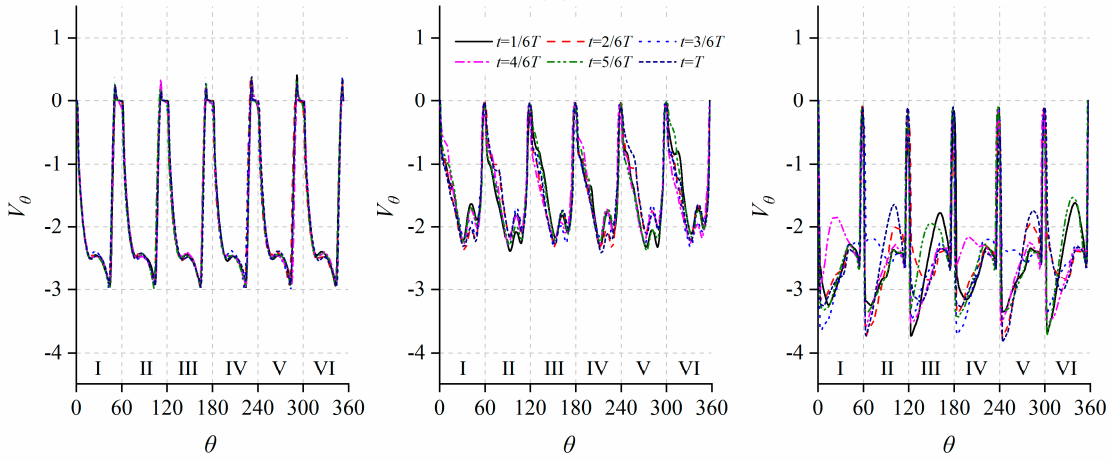
t=1/6T t=2/6T t=3/6T
t=4/6T t=5/6T t=T
V_θ
I II III IV V VI
0 60 120 180 240 300 360
θ

(**c**)

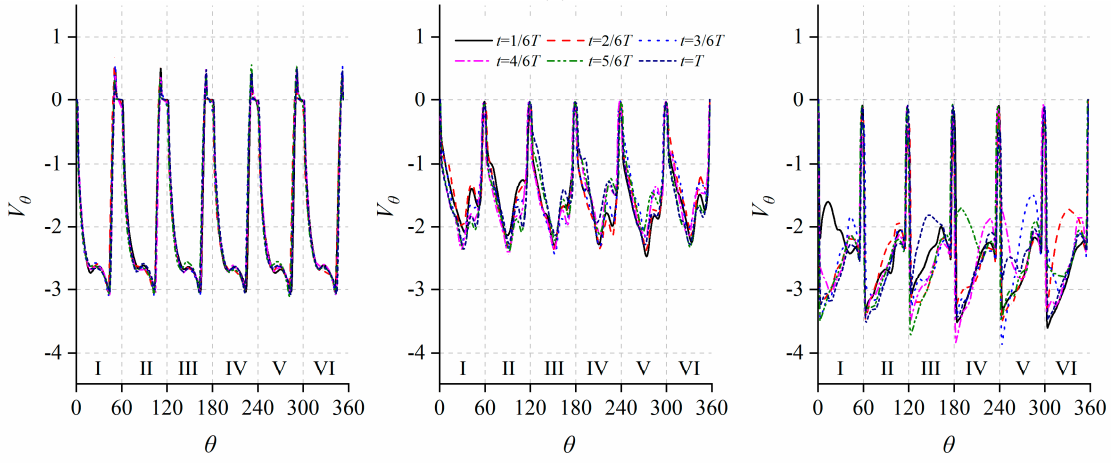
t=1/6T t=2/6T t=3/6T
t=4/6T t=5/6T t=T
V_θ
I II III IV V VI
0 60 120 180 240 300 360
θ

(**d**)

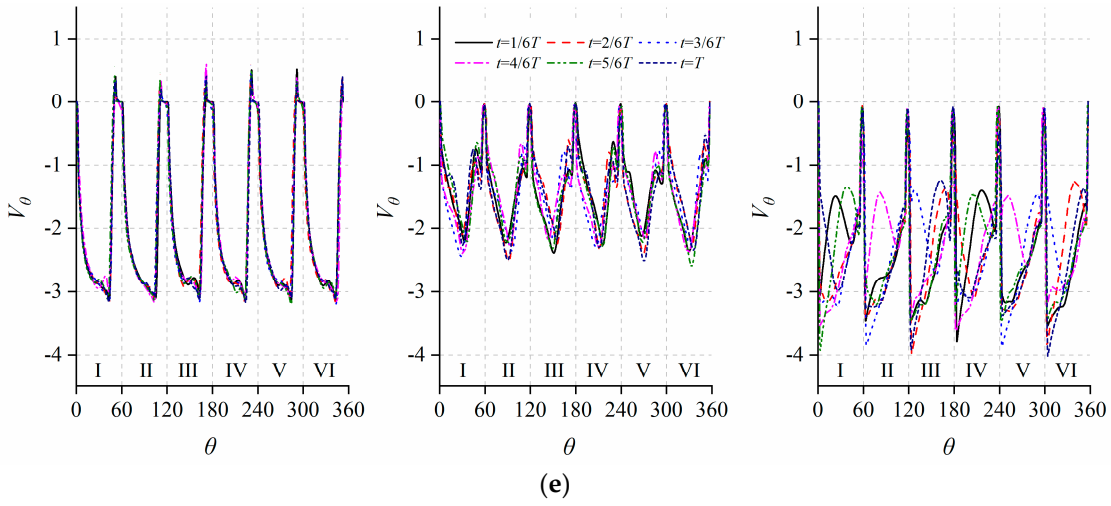

(**e**)

Figure 7. Distributions of instantaneous normalized circumferential velocity along the circumferential direction at r* = 0.0 (left), r* = 0.5 (middle) and r* = 1.0 (right) for (from top to bottom) U_{rot}/U_{ref} = −0.5, −0.3, 0.0, 0.3 and 0.5.

The circumferential velocity shows almost no temporal fluctuation at the leading edge of the blades especially close to the surfaces, and the distributions in various channels are similar. The maximum magnitude for the negative velocity appears close to the suction surface and the value increases with U_{rot} which is the same as that of V_r. Moreover, a positive value of V_θ is clearly observed close to the suction surface for zero-swirling (U_{rot} = 0.0) and counter-rotating ($U_{rot} > 0$) inflow cases, and it gradually becomes obvious as U_{rot} increases. This is generated by the small-scale vortices at the inlet of the channels which restrain the development of flow in the channels and produce the weak circumferential motion of local flow, as is also seen in Figure 4. In the middle region of the channels, the maximum magnitude of negative V_θ reduces compared with flow at the inlet of the channels, and the difference among the various peaks is minor. There is one local peak in the central region of the channel whose magnitude decreases with the value of U_{rot}; for high values of U_{rot}, the fluctuation tends to occupy the whole channel, as revealed by the fluctuation around the suction surface. The flow at the outlet of the channels is highly fluctuating in time for the majority of the channel, and the fluctuation is especially remarkable for the counter-rotating ($U_{rot} > 0$) inflow cases. For the co-rotating ($U_{rot} < 0$) inflow cases, the temporal fluctuation is notably non-uniform especially for the U_{rot} = −0.5 case, i.e., strong in channel-I, channel-II, channel-III and channel-VI but relatively weak in channel-IV and channel-V.

3.4. Three-Dimensional Flow: Hub-to-Shroud Distributions

Since there is a transition of direction for flow from axial to radial in the impeller, the patterns of flow close to the hub and shroud of the impeller differ because of the inertia of flow and possible separation of boundary layer flow on the curved surfaces. The three-dimensionality of internal flow is also reflected by the non-uniformity of velocity across the meridian section of the impeller. In this section, we analyze the three-dimensional flow by its hub-to-shroud distributions of velocity components at two positions as given in Figure 5; the two hub-to-shroud lines locate at r* = 0.5 close to the pressure and suction surfaces of the same channel. The non-dimensional quantity b* is used to denote the local coordinate as the distance measured from the hub, and b* = 0.0 and 1.0 denote the hub and shroud, respectively.

Figure 8 shows the distributions of instantaneous radial velocity V_r on the two hub-to-shroud lines at six equally spaced moments as the impeller rotates for 60°. The curves exhibit temporal variations which are greatly dependent on U_{rot}, and the curves

representing flow adjacent to the surfaces are drastically different depending on the position (pressure or suction surface). For the near-wall flow of pressure surface, the curves vary gently for the co-rotating inflow cases ($U_{rot} < 0$), although the amplitude of variation is noticeable mainly in the central region across the channel. For the zero-swirling inflow case ($U_{rot} = 0.0$), the fluctuation is the most significant at around $b^* = 0.3$, i.e., close to the hub, while it is much smaller in the region close to the shroud. As U_{rot} further increases, the magnitude of instantaneous V_r generally increases in the near-wall regions of hub and shroud, and presents a great fluctuation in the central region of the channel, resulting in an uneven double-peak pattern. The radial velocity of flow near the hub is higher than that of the shroud; this is attributed to the inertia of fluid during the transition of direction as it moves through the channel. The radial velocity in the central region can be nearly zero at a certain moment; we believe that this is induced by the weakly separated flow in the upstream region. The magnitude of V_r for flow close to the suction surface is generally higher. The fluctuating amplitude is quite small in the region very adjacent to the hub and shroud surfaces, while it rapidly increases for flow away from the surfaces. The fluctuation is strongest in the central region of the channel for the co-rotating inflow cases ($U_{rot} < 0$) and comparably weak for the zero-swirling inflow case ($U_{rot} = 0.0$). For counter-rotating inflow cases ($U_{rot} > 0$), the radial velocity fluctuates notably near the hub, and reversed local flow with negative value of V_r appears at certain moments due to the transient evolution of separated vortex.

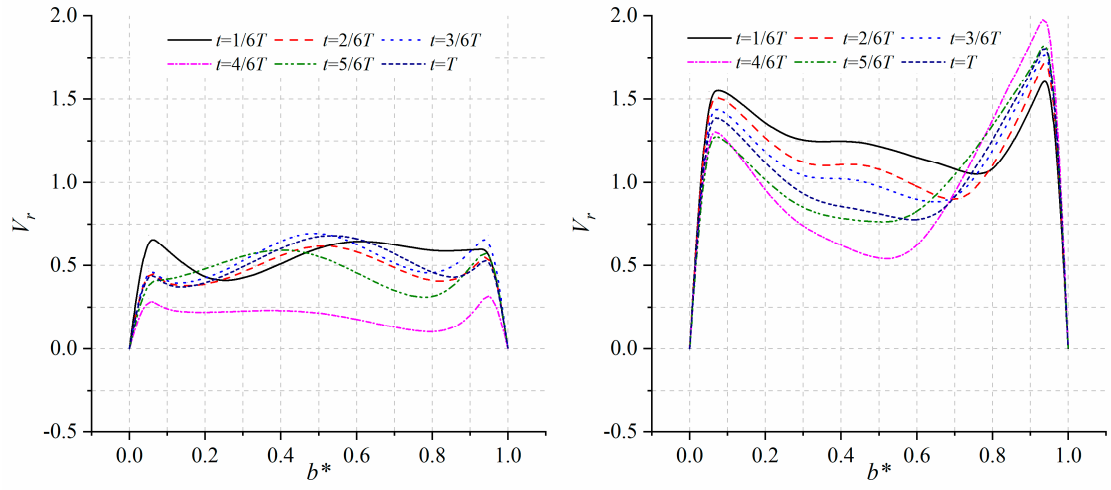

(**a**)

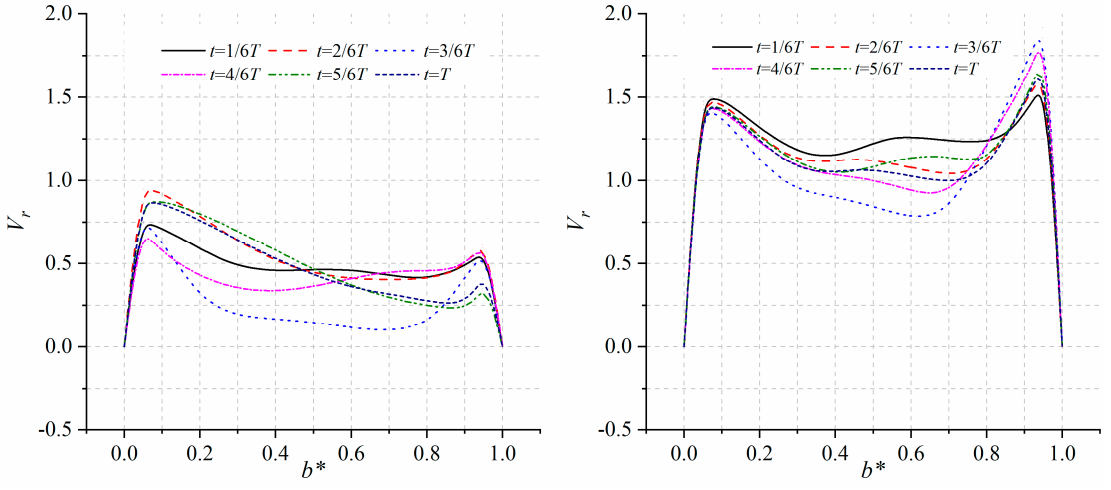

(**b**)

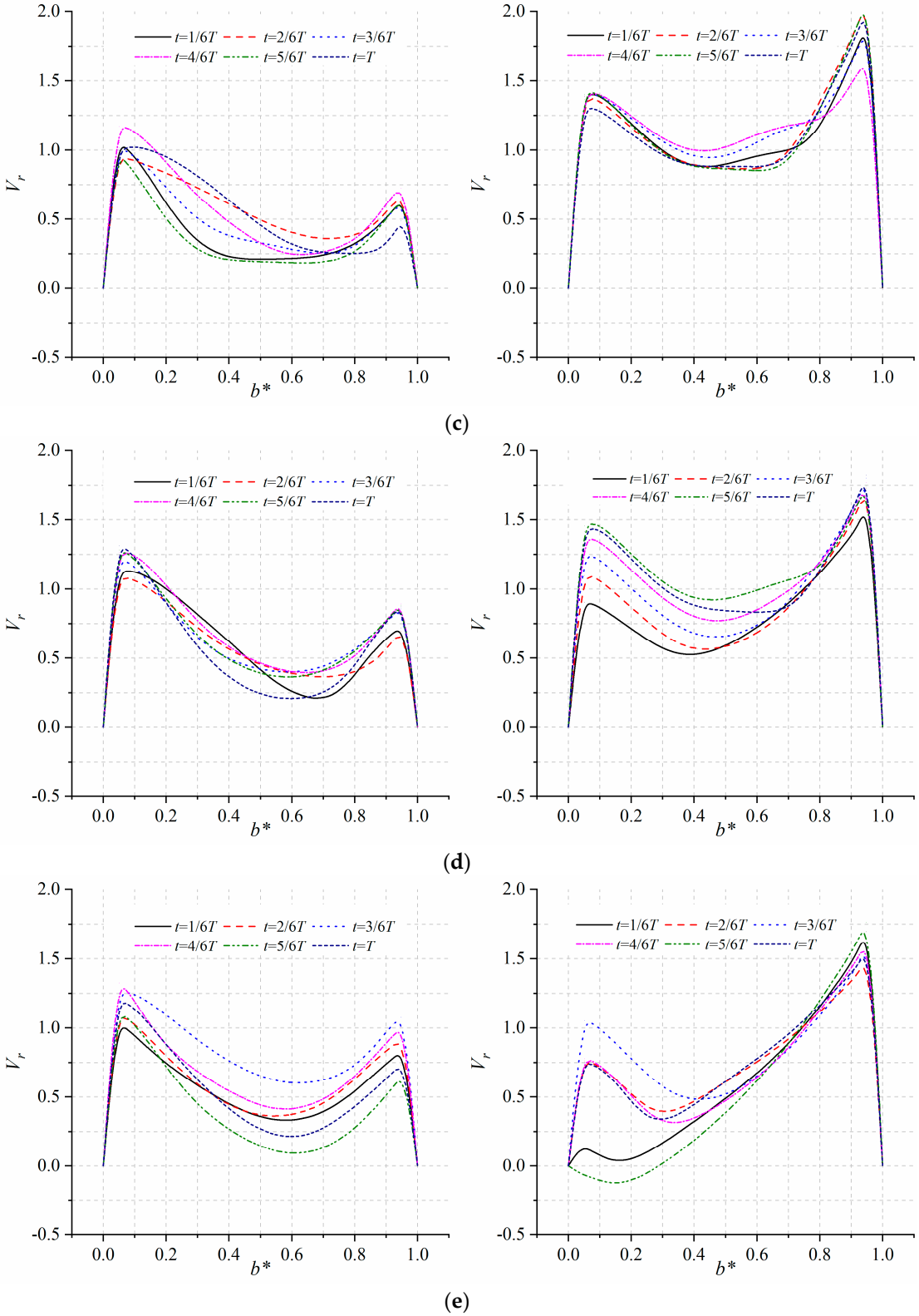

Figure 8. Distributions of instantaneous normalized radial velocity along the hub-to-shroud direction for flow near the pressure surface (left) and suction surface (right) for (from top to bottom) U_{rot}/U_{ref} = −0.5, −0.3, 0.0, 0.3 and 0.5.

The distributions of circumferential velocity V_θ in the hub-to-shroud direction are presented in Figure 9. The temporal variations of V_θ at the two positions differ a lot in

terms of the magnitude, fluctuating amplitude and distribution. The magnitude and temporal variation of V_θ is more uniform for flow near the pressure surface. For flow near the pressure surface, the distribution of V_θ is generally uniform through the whole channel in the hub-to-shroud direction; the magnitude of velocity increases or decreases as a whole such that the fluctuating amplitude at different positions is not substantially different. As U_{rot} increases, the amplitude first decreases until the zero-swirling inflow case and then increases, thus the fluctuation is the most notable for cases of $U_{rot}/U_{ref} = \pm 0.5$. For flow near the suction surface, the distribution of V_θ is obviously non-uniform and the maximum magnitude of negative V_θ generally appears close to the hub. It is found that the co-rotating inflow ($U_{rot} < 0$) results in great fluctuation in the central region and close to the shroud of the channel, while counter-rotating inflow ($U_{rot} > 0$) produces strong fluctuation in the central region and close to the hub of the channel. A consistent reduction in both circumferential and radial velocities is observed for the counter-rotating inflow ($U_{rot} > 0$) cases which is induced by a small-scale vortex generated in the upstream part of the channel and restrains the development of flow towards the outlet.

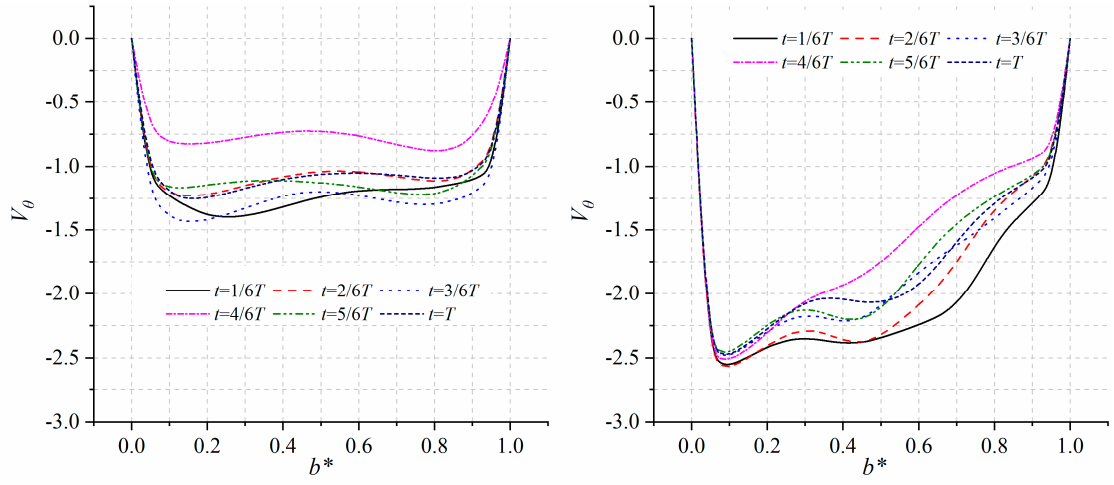

(**a**)

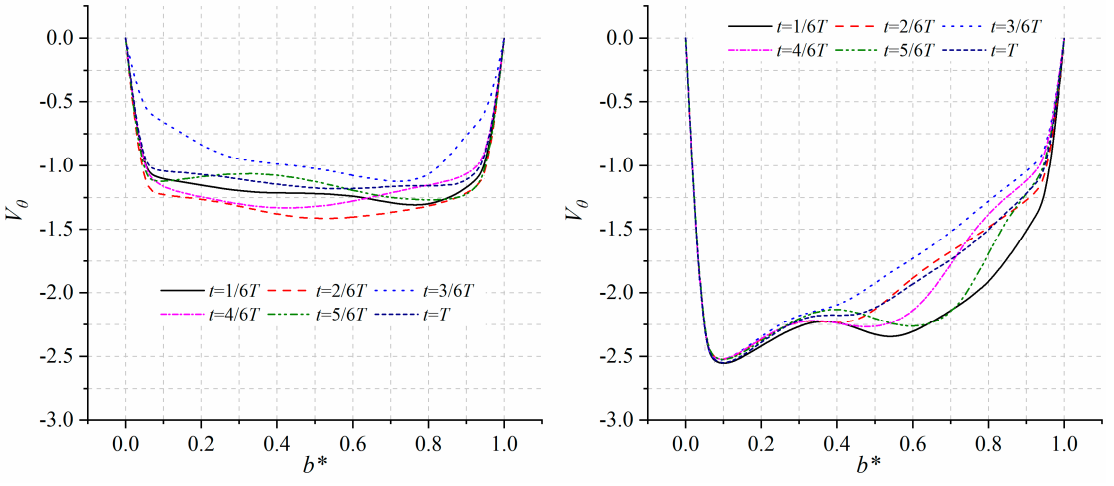

(**b**)

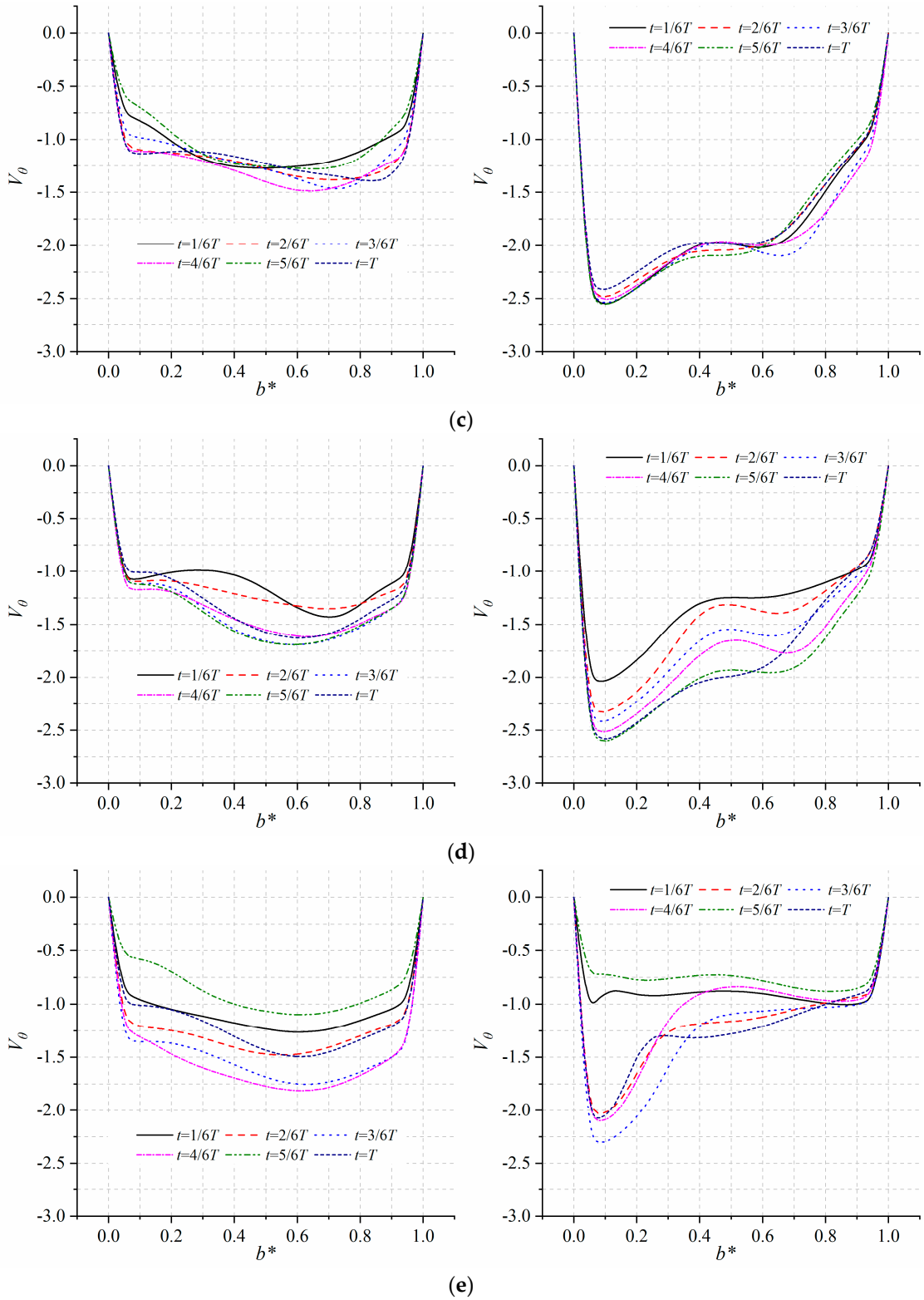

Figure 9. Distributions of instantaneous normalized circumferential velocity along the hub-to-shroud direction for flow near the pressure surface (left) and suction surface (right) for (from top to bottom) U_{rot}/U_{ref} = −0.5, −0.3, 0.0, 0.3 and 0.5.

3.5. Pressure Gradient Field on the Blade Surfaces

The patterns of near-wall flow of the blade are affected by the pressure gradient field on the surfaces; positive and negative pressure gradient could accelerate and decelerate

the local flow. To analyze how the pre-swirl inflow affect the near-wall flow of the blade, Figure 10 presents the distributions of instantaneous pressure coefficient on the mid-span cross-section ($Z/b_2 = 0.5$) from the inlet to outlet of the blade separating channel-I and channel-II at six moments. A local coordinate S is defined on the curved surface of the blade which starts from the leading edge of the blade and ends at the trailing edge, and S_0 is the arc length of the curve, thus $S/S_0 = 0.0$ and 1.0 represent the leading and trailing edges of the blade, respectively.

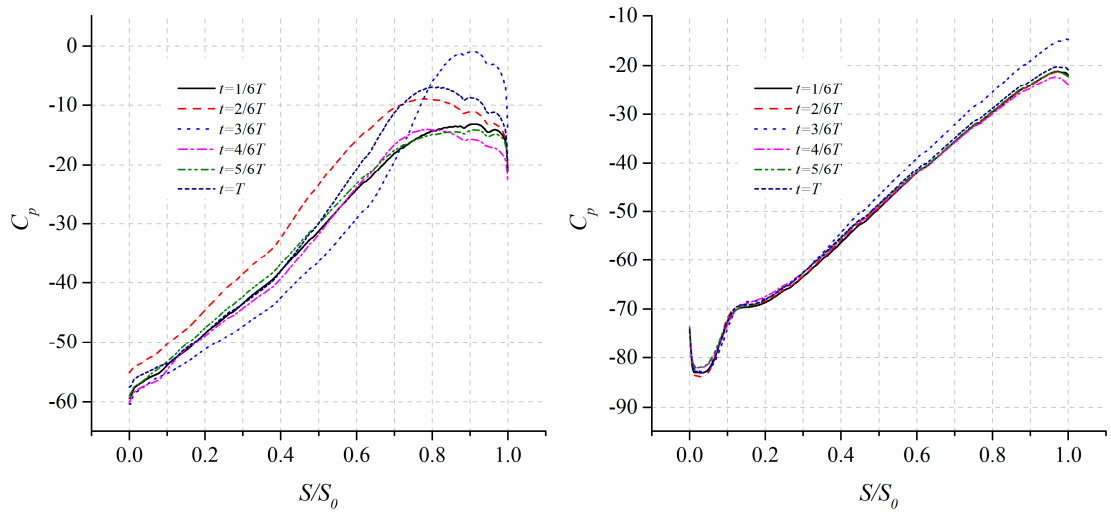

(**a**)

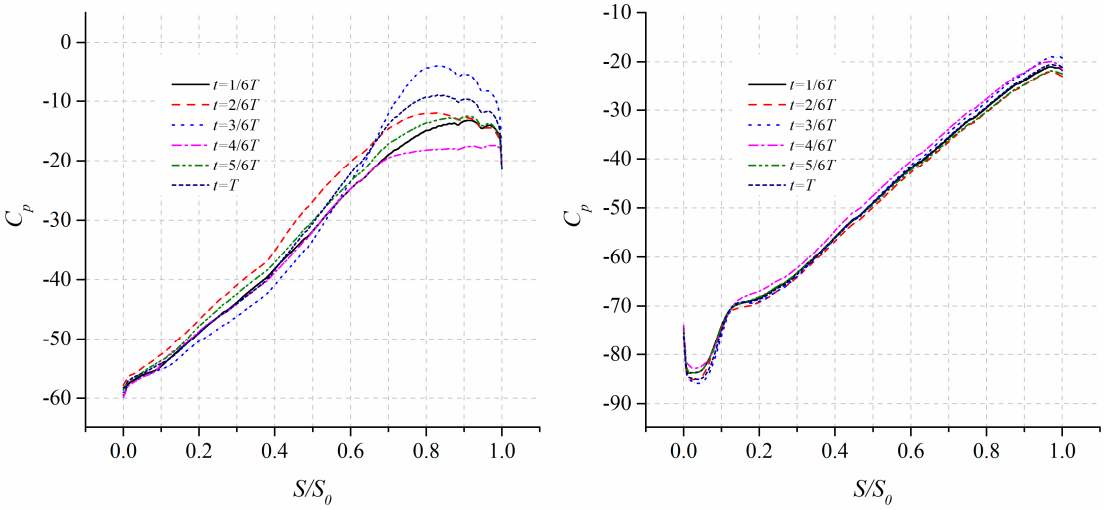

(**b**)

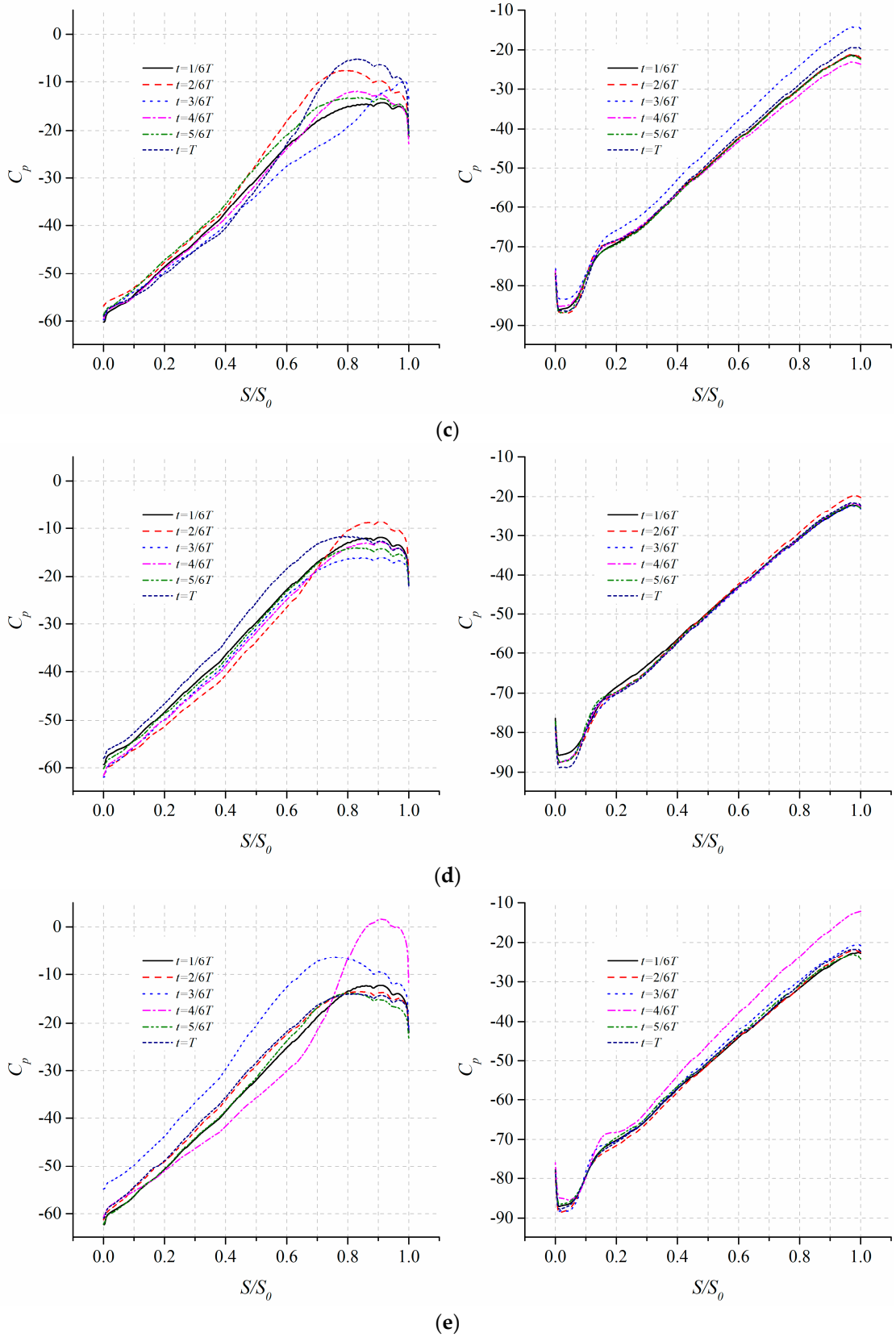

Figure 10. Distribution of pressure coefficient at the mid-span ($Z/b_2 = 0.5$) of pressure surface (left) and suction surface (right) from inlet to outlet of the channel. The curves are plotted (from top to bottom) at $U_{rot}/U_{ref} = -0.5, -0.3, 0.0, 0.3$ and 0.5.

It is seen that both the pressure and suction surfaces of the blade are occupied by the adverse pressure gradient (APG) field. On the pressure surface, the pressure coefficient monotonically increases from the leading edge and reaches maximum at around S/S_0 = 0.8–0.9, and then slightly decreases until the trailing edge. However, it is observed in Figure 4 that there is no separation because of the weak APG field. The fluctuation of pressure coefficient is relatively strong for cases of inflow with higher Urot, especially in the upstream and middle section of the pressure surface S/S_0 = 0.0–0.7, while the pre-swirl inflow has no obvious influence on the pressure coefficient in the remained part of the surface. The pressure coefficient on the suction surface of the blade exhibit entirely different distributions. It decreases right at the leading edge and then recovers until the trailing edge, thus the suction surface is almost entirely occupied by APG which decelerates the boundary layer flow along with the viscous drag. It is seen in Figure 5 that small-scale vortices are generated on the suction surface of the leading edge, and moves towards the outlet of impeller while the size and intensity do not vary a lot.

3.6. Topology of Limiting Streamlines

The three-dimensionality of boundary layer flow on the surfaces of the blade reflects the patterns of possible separation and reattachment. Figure 11 shows the distribution of instantaneous limiting streamlines on the pressure and suction surfaces of the blade located between channel-I and channel-II. The sinks and sources of the streamlines represent the separation and reattachment of local boundary layer flow. It is seen that separation and reattachment of flow, although weak as seen in Figure 4, occur around the leading edge of the blade, while the boundary layer flow in the middle and downstream sections of the blade is stable. The pre-swirl inflow does not have any noticeable effect on the patterns of separation and reattachment, especially for the pressure surface. However, the patterns of reattachment on the suction surface are also determined by the corner flow between the surface and the hub/shroud of the impeller. It is noticed that for the zero-swirling inflow case (U_{rot} = 0.0), reattachment also occurs at the central region of the suction surface. Therefore, it is believed that for the counter-rotating inflow cases (U_{rot} > 0), the separation and reattachment on the blade surfaces can be effectively reduced which improves the uniformity of the flow.

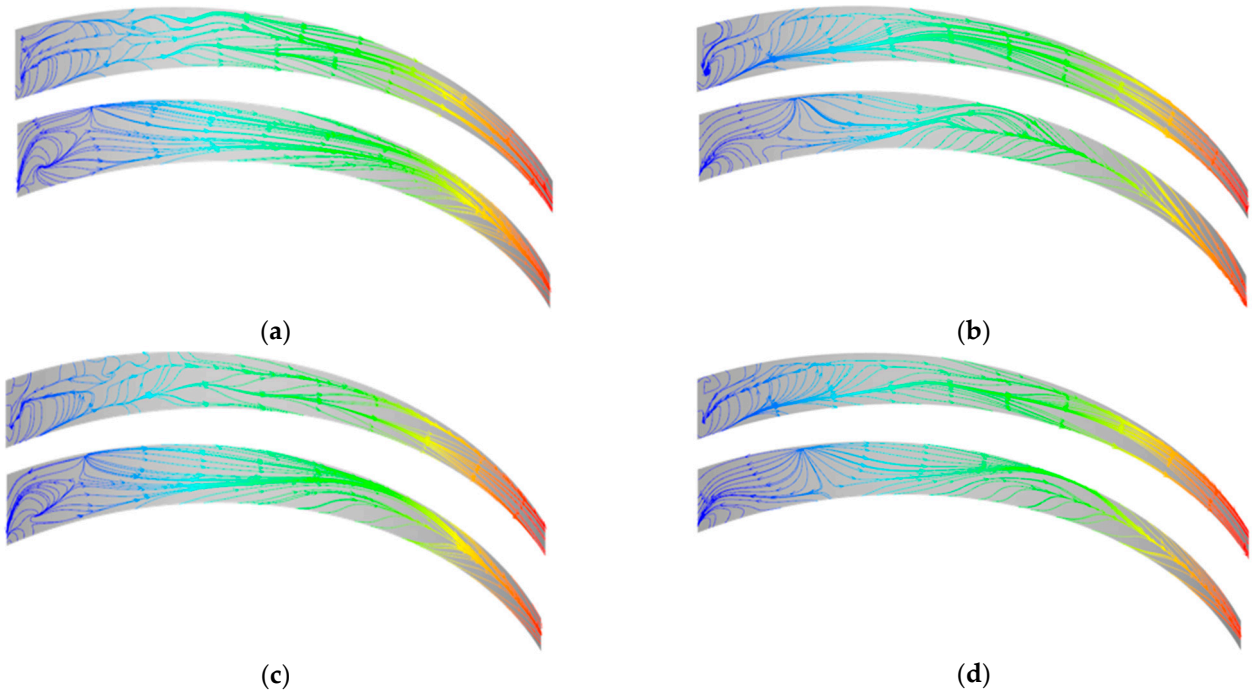

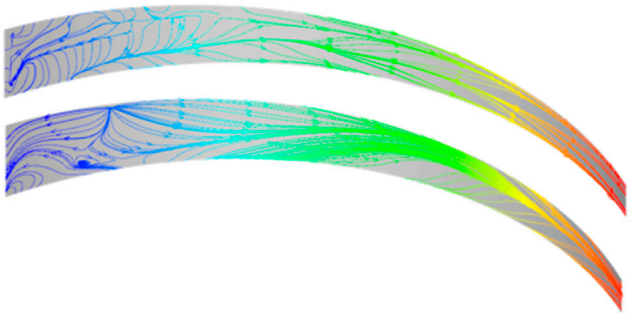

(**e**)

Figure 11. Instantaneous limiting streamlines on the pressure (top) and suction (bottom) surfaces of the blade for (from (**a**) to (**e**)) U_{rot}/U_{ref} = −0.5, 0.5, −0.3, 0.3 and 0.0.

4. Conclusions

This work presents a numerical investigation on the transient characteristics of three-dimensionality of internal flow in a centrifugal impeller perturbed by simple pre-swirl inflow. The influences of co-rotating and counter-rotating inflow under the designed flow rate are explored using the URANS approach. The following conclusions are obtained:

(1) The temporal fluctuation of flow is weak at the inlet of the blade channels (r^* = 0.0). Close to the suction surface, the magnitude of radial velocity V_r for the counter-rotating inflow is 15–25% larger compared to the co-rotating inflow cases. The peak magnitude reaches the maximum about 2.5 m/s near the suction surface. In the middle of the channels (r^* = 0.5), the peak magnitude of V_r moves from suction to pressure surface as the inflow gets from co-rotating to counter-rotating, and the fluctuating amplitude greatly increases, and the magnitude of V_r varies from 0 to 1.2 m/s. The fluctuation is highest at the outlet of the channels (r^* = 1.0) especially for the counter-rotating inflow cases. The magnitude of circumferential velocity V_θ reaches the minimum in the central channel for the counter-rotating inflow cases, and the minimum value reaches about 2.2 m/s.

(2) The internal flow of the impeller is highly three-dimensional in the hub-to-shroud direction. The strongest fluctuation of V_r occurs in the central region of the channel for the co-rotating inflow cases, while the peak is observed close to the hub for the counter-rotating inflow cases which can be negative as a result of the separated vortex. Close to the hub, compared to the zero-swirling inflow, the magnitude of V_r near the pressure surface is smaller for the co-rotating inflow cases and the degree of reduction increases with the increase in rotating speed, while for the counter-rotating inflow cases the magnitude of V_r reaches 1.25 m/s, which is 25% larger for the zero-rotating inflow cases. On the contrary, near the suction surface the magnitude of V_r is smaller for the counter-rotating inflow cases about 50–75%, compared to the co-rotating cases. For the circumferential velocity V_θ, great fluctuation appears in the central region and close to the shroud for the co-rotating inflow cases, while in the central region and close to the hub for the counter-rotating cases.

(3) Both pressure and suction surfaces of the blade are mainly occupied by an adverse pressure gradient field. There is no obvious separation on the pressure surfaces because of the weak APG, and small-scale vortices appear on the suction surface around the leading edge.

(4) Three-dimensional separation and reattachment of flow occur around the leading edge of the blade are observed by the limiting streamlines, while the internal flow is quite stable and uniform in the middle and downstream sections of the channels. Reattachment also occurs at the central region of the suction surface for the zero-swirling inflow, and the counter-rotating inflow could reduce the reattachment which improves the uniformity of the internal flow.

The primary objective of this work was to present and analyze the transient characteristics of three-dimensional internal flow of a centrifugal impeller as perturbed by simply constructed pre-swirl inflow, and to reveal the influence of the pre-swirl inflow. The findings and conclusions may be helpful in the design of a pump system involving a curved inflow tube or guide vanes system for the improved efficiency and operational stability of the impeller. Since the pre-swirl inflow is simple in pattern, the significance of present study is limited, and we would analyze the influence of realistic guide vanes which generate non-uniform and fluctuating wake flow in future works.

Author Contributions: Conceptualization, Z.W. and W.Z.; data curation, Z.W.; formal analysis, Z.W. and W.Z.; funding acquisition, W.Z.; investigation, Z.W. and W.Z.; methodology, Z.W.; project administration, W.Z.; resources, W.Z.; software, Z.W.; supervision, W.Z.; validation, Z.W.; visualization, Z.W.; writing—original draft, Z.W.; writing—review and editing, W.Z. All authors have read and agreed to the published version of the manuscript.

Funding: This work was supported by Natural Science Foundation of China (52176047), Zhejiang Province Science and Technology Plan Project (2020C04011, 2022C01227) and 111 Project (D21011).

Institutional Review Board Statement: Not applicable.

Informed Consent Statement: Not applicable.

Data Availability Statement: Not applicable.

Conflicts of Interest: The authors declare no conflict of interest.

References

1. Byskov, R.K.; Jacobsen, C.B.; Pedersen, N. Flow in a centrifugal pump impeller at design and off-design conditions-Part I: Particle image velocimetry (PIV) and laser Doppler velocimery (LDV) measurements. *J. Fluids Eng*. **2003**, *125*, 61–72. https://doi.org/10.1115/1.1524585.
2. Byskov, R.K.; Jacobsen, C.B.; Pedersen, N. Flow in a centrifugal pump impeller at design and off-design conditions-Part II: large eddy simulations. *J. Fluids Eng*. **2003**, *125*, 73–83. https://doi.org/10.1115/1.1524586.
3. Zhang, N.; Jiang, J.; Gao, B.; Liu, X. DDES analysis of unsteady flow evolution and pressure pulsation at off-design condition of a centrifugal pump. *Renew Energ*. **2020**, *153*, 193–204. https://doi.org/10.1016/j.renene.2020.02.015.
4. Zhang, N.; Gao, B.; Ni, D.; Liu, X. Coherence analysis to detect unsteady rotating stall phenomenon based on pressure pulsation signals of a centrifugal pump. *Mech. Syst. Signal Pract*. **2021**, *148*, 107161. https://doi.org/10.1016/j.ymssp.2020.107161.
5. Krause, N.; Zähringer, K.; Pap, E. Time-resolved particle imaging velocimetry for the investigation of rotating stall in a radial pump. *Exp. Fluids* **2005**, *39*, 192–201. https://doi.org/10.1007/s00348-005-0935-2.
6. Ullum, U.; Wright, J.; Dayi, O.; Ecder, A.; Soulaimani, A.; Piché, R.; Kamath, H. Prediction of rotating stall within an impeller of a centrifugal pump based on spectral analysis of pressure and velocity data. *Phys. Conf. Ser*. **2006**, *52*, 004. https://doi.org/10.1088/1742-6596/52/1/004.
7. Zhou, P.; Dai, J.; Yan, C.; Zheng, S.; Ye, C.; Zhang, X. Effect of Stall Cells on Pressure Fluctuations Characteristics in a Centrifugal Pump. *Symmetry* **2019**, *11*, 1116. https://doi.org/10.3390/sym11091116.
8. Zhou, P.-J; Wang, F.-J.; Yang, Z.-J.; Mou, J-G. Investigation of rotating stall for a centrifugal pump impeller using various SGS models. *J. Hydrodyn. Ser. B* **2017**, *29*, 235–242. https://doi.org/10.1016/S1001-6058(16)60733-3.
9. Pei, J.; Yuan, S.-Q.; Li, X.-J.; Yuan, J.-P. Numerical prediction of 3-D periodic flow unsteadiness in a centrifugal pump under part-load condition. *J. Hydrodyn*. **2014**, *26*, 257–263. https://doi.org/10.1016/S1001-6058(14)60029-9.
10. Li, X.; Chen, B.; Luo, X.; Zhu, Z. Effects of flow pattern on hydraulic performance and energy conversion characterisation in a centrifugal pump. *Renew Energ*. **2020**, *151*, 475–487. https://doi.org/10.1016/j.renene.2019.11.049.
11. Westra, R.W.; Broersma, L.; Van Andel, K.; Kruyt, N.P. Secondary flows in centrifugal pump impellers: PIV measurements and CFD computations. In Proceedings of the ASME 2009 Fluids Engineering Division Summer Meeting, Vail, CO, USA, 2–6 August 2009; Volume 43727, pp. 305–314. https://doi.org/10.1115/FEDSM2009-78275.
12. Song, Z.; Li, X.; Liu, Z. Research on the mechanism of the influence of inlet pre-rotation on the aerodynamic performance of centrifugal impeller. *Chin. J. Appl. Mech*. **2021**, *38*, 53–59. http://dx.chinadoi.cn/10.11776/cjam.38.01.A063.
13. Xiao, J.; Gu, C.; Gao, C.; Shu, X.W. Numerical analysis of the flow in centrifugal compressor in consideration of inlet pre-whirl. *Chin. J. Power Eng*. **2008**, *28*, 400–403. http://dx.chinadoi.cn/10.3321/j.issn:1000-6761.2008.03.014.
14. Gish, L.A.; Carandang, A.; Hawbaker, G. Experimental evaluation of a shrouded horizontal axis hydrokinetic turbine with pre-swirl stators. *J. Ocean Eng*. **2020**, *204*, 107252. https://doi.org/10.1016/j.oceaneng.2020.107252.
15. Danlos, A.; Podevin, P.; Toussaint, M. Pre-swirl mechanism in front of a centrifugal compressor: effects on surge line and on unsteady phenomena in surge area. *MATEC Web Conf*. **2017**, *133*, 04002. https://doi.org/10.1051/matecconf/201713304002.

16. Amin, I.; Xiao, Q. Numerical simulation of a horizontal axis tidal turbine with a pre-swirl stator. *Dev. Marit. Transp. Exploit. Sea Resour.* **2014**, *2014*, 863–869. http://dx.doi.org/10.1201/b15813-109.
17. Mohseni, A.; Goldhahn, E.; Van den Braembussche, R.A.; Seume, J.R. Novel IGV designs for centrifugal compressors and their interaction with the impeller. *J. Turbomach.* **2012**, *134*, 021006. https://doi.org/10.1115/1.4003235.
18. Zhang, K.; Tan, M.; Wu, X.; Ma, H.; Liu, X. Clocking effect of guide vane in multi-stage centrifugal pump. *J. Drain. Irrig. Mach. Eng.* **2021**, *39*, 663–670. Available online: https://t.cnki.net/kcms/detail/32.1814.th.20210624.1113.006.html (accessed on 24 July 2021).
19. Zhao, J.; Wang, Z.; Xi, G.; Zhao, Y. Improvements of inlet structure and sweep-angle of guide vane inside a centrifugal compressor at large pre-swirl. *J. Xi'an Jiaotong Univ.* **2017**, *54*, 1–6. http://dx.doi.org/10.7652/xjtuxb201711001.
20. Xu, L.; Ji, D.; Shi, W.; Xu, B.; Lu, W.; Lu, L. Influence of inlet angle of guide vane on hydraulic performance of an axial flow pump based on CFD. *Shock Vib.* **2020**, *2020*, 1–16. http://dx.doi.org/10.1155/2020/8880789.
21. Poujol, N.; Trébinjac, I.; Duquesne, P. Effects of inlet guide vanes on the performance and stability of an aeronautical centrifugal compressor. *J. Turbomach.* **2021**, *143*, 101010. https://doi.org/10.1115/1.4050944.
22. Zhong, L.; Min, G.; Xiao, K. Experimental study of guide vane influence on performance of axial-flow pump. *J. Drain. Irrig. Mach. Eng.* **2009**, *27*, 15–18. Available online: https://www.researchgate.net/publication/286887847 (accessed on 30 January 2009).
23. Liu, Z.; Yang, H.; He, H.; Yu, P.; Wei, Y.; Zhang, W. Flow instability in a volute-free centrifugal fan subjected to non-axisymmetric pre-swirl flow from upstream bended inflow tube. *Proc. Inst. Mech. Eng. Part A J. Power Energy* **2022**, *236*, 689–713. https://doi.org/10.1177/09576509211062664.
24. Heidarian, A.; Ghassemi, H.; Liu, P. Numerical Analysis of the Effects of Riblets on Drag Reduction of a Flat Plate. *Appl. Fluid Mech.* **2018**, *11*, 3. https://dx.doi.org/10.29252/jafm.11.03.28344.
25. Jiang, Q.; Heng, Y.; Liu, X.; Zhang, W.; Bois, G.; Si, Q. A Review of Design Considerations of Centrifugal Pump Capability for Handling Inlet Gas-Liquid Two-Phase Flows. *Energies* **2019**, *12*, 1078. https://doi.org/10.3390/en12061078.
26. Heidarian, A.; Ghassemi, H.; Liu, P. Numerical Aerodynamic of the Rectangular Wing Concerning to Ground Effect. *Am. J. Mech. Eng.* **2018** ,*6*, 43–47. https://doi.org/10.12691/ajme-6-2-1.
27. Xu, Y.; Liu, P.; Penesis, I.; He, G.; Heidarian, A.; Ghassemi, H. Energy Generation Efficiency and Strength Coupled Design and Optimization of Wind Turbine Rotor Blades. *J. Energ. Eng.* **2019**, *145*, 04019004. https://orcid.org/0000-0003-2158-5442.
28. Cai, J.; Wang, Y.; Yu, S. The Recent Progress and the State-of-art Applications of Navier Stokes Equation. *Highlights Sci. Eng. Technol.* **2022**, *12*, 114–120. https://doi.org/10.54097/hset.v12i.1413.
29. Menter, F.R.; Kuntz, M.; Langtry, R. Ten years of industrial experience with the SST turbulence model. *Turbul. Heat Mass Transf.* **2003**, *4*, 625–632. Available online: https://www.researchgate.net/publication/228742295 (accessed on January 2003).
30. Menter, F.R. Influence of freestream values on k-omega turbulence model predictions. *AIAA J.* **1992**, *30*, 1657–1659. https://doi.org/10.2514/3.11115.
31. Menter, F.R. Two-equation eddy-viscosity turbulence models for engineering applications. *AIAA J.* **2012**, *32*, 8 https://doi.org/10.2514/3.12149.
32. Wilcox, D.C. Reassessment of the scale-determining equation for advanced turbulence models. *AIAA J.* **2012**, *26*, 11. https://doi.org/10.2514/3.10041.